Journal of
Nanoscience and Nanotechnology
Vol. 18, 7319–7334, 2018
www.aspbs.com/jnn

Recent Advances in Properties, Synthesis and Applications of Two-Dimensional HfS_2

Denggui Wang, Xingwang Zhang*, and Zhanguo Wang

Key Lab of Semiconductor Materials Science, Institute of Semiconductors, Chinese Academy of Sciences, Beijing 100083, and College of Materials Science and Opto-Electronic Technology, University of Chinese Academy of Sciences, Beijing 100049, China

As a member of transition metal dichalcogenides (TMDs) family, two-dimensional (2D) hafnium disulphide (HfS_2) has attracted significant interest because of its excellent properties, including reasonable bandgap, ultrahigh room-temperature mobility and sheet current density, and definite chemical stability, which make 2D HfS_2 a potential candidate material for future electronic and or optoelectronic devices. This review mainly focuses on the recent progress in the properties, synthesis and applications of 2D HfS_2. Following a brief introduction on the structure of HfS_2, we present its bandgap and electrical properties, as well as chemical stability. Up to now, analogously to what has been implemented for graphene, various synthesis techniques, such as mechanical exfoliation and chemical vapor deposition (CVD), have been developed to prepare ultrathin 2D HfS_2 layers, and the advantages and limitations of each method are presented along with addition of personal insights. Meanwhile, diverse characterization methods of 2D HfS_2 are listed and discussed, which are quite useful for uncovering the correlations between structures and properties. Then, we thoroughly illustrate the existing and potential applications of 2D HfS_2, especially focusing on the field of field-effect transistors, photodetectors and phototransistors. Finally, current status and future prospects for this emerging material are discussed.

Keywords: HfS_2, Two-Dimensional, Properties, Preparation, Applications.

CONTENTS

1. INTRODUCTION

Inspired by the discovery of mechanically exfoliated graphene in 2004,[1] research on ultrathin two-dimensional (2D) layered materials has grown exponentially throughout different fields, including material science, chemistry, physics, engineering and nanotechnology. Graphene is the hexagonal arrangement of carbon atoms forming a one-atom thick planar sheet that exhibits various fascinating properties,[2] such as ultrahigh carrier mobility,[3–5] excellent optical transparency,[6] prominent Young's modulus,[7–8] and outstanding thermal conductivity.[9] However, the absence of an intrinsic band gap is the fatal drawback of graphene,[10] which limits its applications as the semiconducting active layer in electronics and optoelectronics devices. For such applications, scientific attention is focusing on other 2D materials with sizable bandgaps, such as black phosphorus,[11–20] hexagonal boron nitride (h-BN),[21–35] and transition metal dichalcogenides (TMDs).[36–55]

2D TMDs are usually denoted as MX_2, where M is a transition metal (Mo, W, Hf, and so on) and X is a chalcogen (group VIA; S, Se, Te). Transition metals ranging from group IVB to group VIIB have different numbers of *d* electrons, which fill up the nonbonding *d* bands to different levels, resulting in varied electronic properties including insulating, semiconducting,

*Author to whom correspondence should be addressed.

 1533-4880/2018/18/7319/016 doi:10.1166/jnn.2018.16042

metallic, and superconducting.[37–39] Recently, TMDs, as an important and abundant class of 2D layered materials, have attracted tremendous attention owning to their ultimate body thickness, sizable and tunable band gap, and decent theoretical room-temperature mobility. These infusive properties have created unprecedented opportunities to open up new fundamental research and technological innovation.

As a member of the group IVB TMDs family, hafnium disulphide (HfS_2) is theoretically predicted to have many interesting properties,[56–74] including ultrahigh room-temperature mobility[64] and sheet current density,[65] which is suitable for the applications of transistors,[75–84] photodetectors[85–87] and photocatalyst,[69, 70] especially catering to circuits requiring low stand-by power in the future. However, to our knowledge, even motivated by the rapid progress in the field of layered TMDs, there exists no review article on 2D HfS_2. Therefore, we wish to address the gap in the literature by conducting a comprehensive review of the HfS_2.

In this tutorial review, we aim to introduce the recent progress in the properties, synthesis and applications of HfS_2. Firstly, we will give a brief summary of the excellent properties of 2D HfS_2. Then we will discuss various approaches for the synthesis of 2D HfS_2. Similar to the well-known techniques utilized for the growth of graphene, some methods have been employed to synthesize 2D HfS_2 crystal. Meanwhile, the diverse characterization approaches of 2D HfS_2 will be presented. After that, we will thoroughly illustrate the existing and potential applications of 2D HfS_2 in the electronics and optoelectronics. In the end, we will give some personal insights into the current challenges and future opportunities in this promising field.

2. PROPERTIES OF 2D HfS_2

2D HfS_2 exhibits a unique combination of advantageous properties, including reasonable bandgap, excellent carrier mobility, high sheet current density, and definite chemical stability. These unique properties make 2D HfS_2 a

Denggui Wang received his B.S. Degree in 2014 from University of Science and Technology of China. He is a Ph.D. candidate student under the supervision of Professor X. W. Zhang of Key Lab of Semiconductor Materials Science, Institute of Semiconductors, Chinese Academy of Sciences (CAS). His current research interest focuses on the synthesis of transition metal dichalcogenides and their applications in optoelectronic devices.

Xingwang Zhang received his Bachelor of Science in Physics from Lanzhou University in 1994 and Ph.D. degree in Condensed Matter Physics from the same university in 1999. He did post-doctor study at the Chinese University of Hong Kong (CUHK) from 1999 to 2001. He worked in succession as a visiting scientist and a Humboldt Research Fellow in University of Ulm, Germany from 2001 to 2004. After that he joined the Key Lab of Semiconductor Materials Science, Institute of Semiconductors, Chinese Academy of Sciences as a full professor. His current research interests include 2D atomic crystals, photovoltaic materials and devices.

Zhanguo Wang graduated from Department of Physics, Nankai University, China in 1962. Then he immediately joined the Institute of Semiconductors, Chinese Academy of Sciences (IS, CAS); there he was engaged in studies on semiconductor materials physics and materials characterization till 1980. From 1980 to 1983, he was as a visiting scientist at Department of Solid State Physics, the University of Lund, Sweden, where he contributed to photoluminescence and deep level physics studies of semiconductors. He became a professor in 1986 and was elected as a member of the CAS in 1995. From 1994 till now, his research work has concentrated to strain induced self-organized GaAs sand InP based quantum wires and quantum dot as well as quantum cascade structures growth and quantum devices fabrication. He has published more than 180 refereed papers in many authoritative journals since 1984. And he was awarded a number of prizes from the Nation and Chinese Academy of Sciences.

promising candidate for a rich variety of applications. In this section, the structure and various properties will be described in detail.

2.1. Structure

TMDs share a similar layered structure of the form X–M–X, with the chalcogen atoms in two hexagonal planes separated by a plane of metal atoms.[37–39] It should be pointed out that a single layer X–M–X exhibits only two polymorphs: trigonal prismatic (1H) and octahedral (1T) phases.[39] The former belongs to the D_{3h} point group, whereas the latter belongs to the D_{3d} group. The adjacent strongly bonded layers are held together by weak van der Waals interactions to form the bulk crystal in a variety of polytypes: 2H (hexagonal symmetry, two layers per repeat unit, trigonal prismatic coordination), 3R (rhombohedral symmetry, three layers per repeat unit, trigonal prismatic coordination) and 1T (tetragonal symmetry, one layer per repeat unit, octahedral coordination),[37] as shown in Figure 1(a).

HfS_2 layered crystals have the CdI_2-type structure (1T structure) with the corresponding space group *P-3m1*.[59] Hafnium atoms are octahedrally coordinated by six sulfur atoms, and the second sulfur atomic layer is rotated by 60° with respect to the first S layer in the S–Hf–S sandwich structure (Figs. 1(b and c)). Therefore, the lattice constant c is spanned by only one sandwich layer, and the crystal parameters are $a = b = 3.63$ Å and $c = 5.85$ Å.[56,59] As van der Waals packed layered material, ultrathin HfS_2 can be prepared by mechanical exfoliation from bulk single crystals, thus providing the possibility to explore the physical properties at the 2D monolayer limit.

2.2. Bandgap

Regarding the electronic and optoelectronic applications, bandgap is one of the most important parameters in any 2D semiconductors. To address the promising properties of 2D HfS_2, first-principles calculations have been widely performed to study its electronic band structures. The electronic structures of monolayer HfS_2 through density functional theory (DFT) suggest that the highly anisotropic conduction band (CB) with its minimum located at the M point, and the calculated indirect bandgap of HfS_2 is 1.13 eV.[76] In addition, Zhao et al. predicted that the indirect bandgap of monolayered HfS_2 is 1.29 eV via Perdew-Burke-Ernzerhof (PBE) hybrid functional methods, whereas Rasmussen et al. showed that the indirect bandgap of freestanding HfS_2 monolayer is 2.98 eV by using the local density approximation (LDA) and G_0W_0 calculations.[67,74] The difference from aforementioned calculated bandgaps for HfS_2 layer may result from the different pseudo potentials and ground state structures used

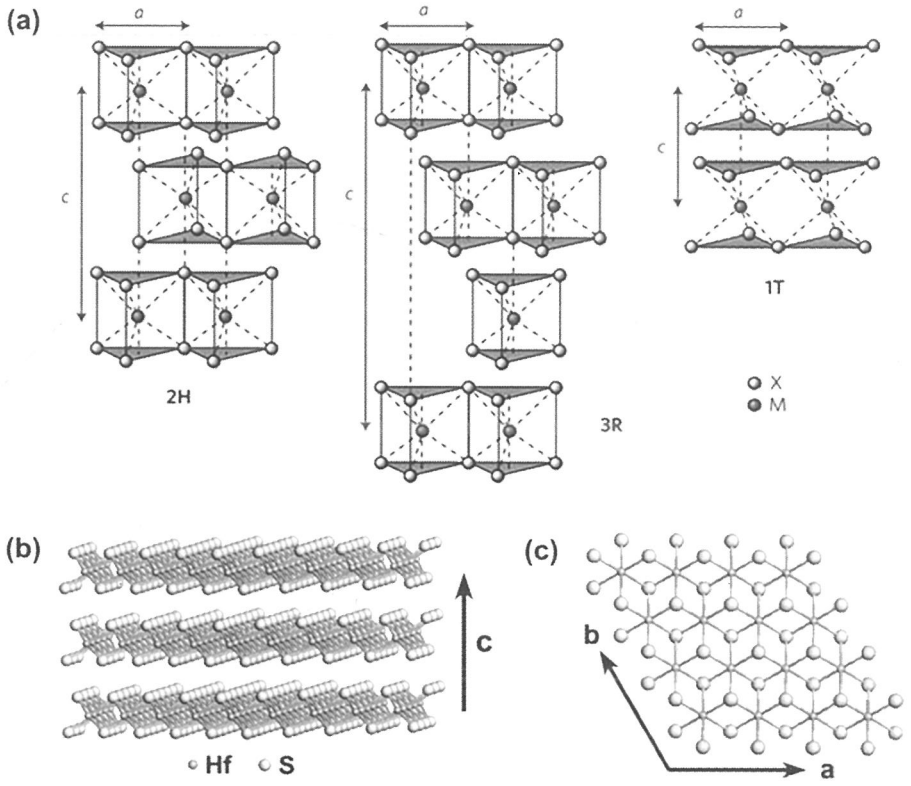

Figure 1. (a) Schematics of the structural polytypes: 2H, 3R and 1T. (b) Side and (c) top views of the hexagonal structure of HfS_2. Reprinted with permission from [37], Q. H. Wang, et al., *Nat. Nanotechnol.* 7, 699 **(2012)**. © 2012, Nature Publishing Group; From [86], D. G. Wang, et al., *2D Mater.* 4, 031012 **(2017)**. © 2017, IOP Publishing.

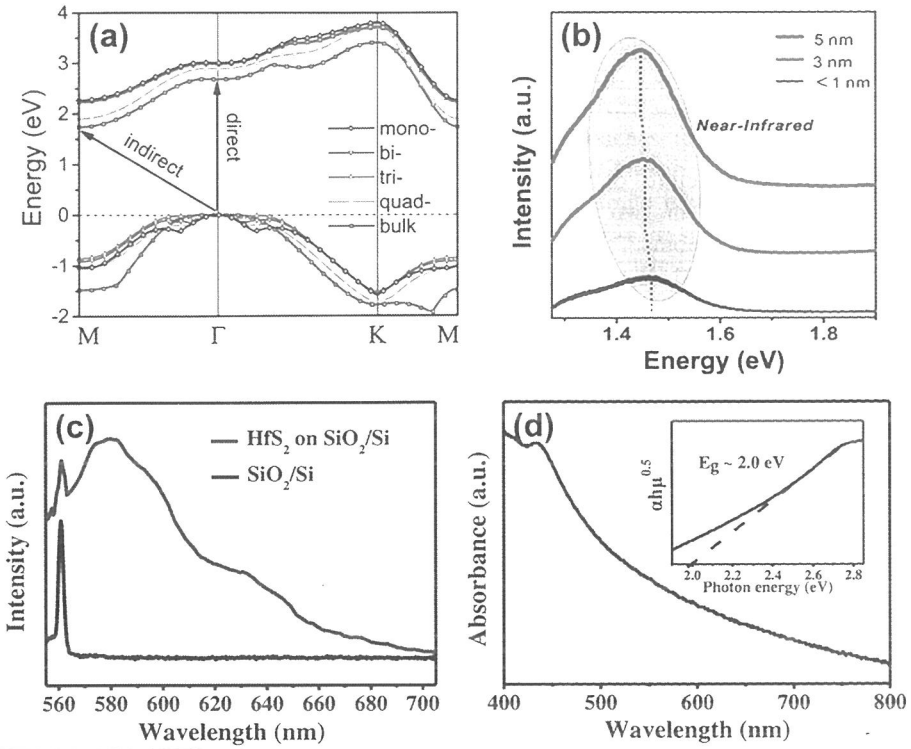

Figure 2. (a) The top of valence band and bottom of conduction band of mono-, bi-, tri-, quad-layer and bulk HfS_2. PL spectra of HfS_2 layers on (b) mica and (c) SiO_2/Si substrates, respectively. (d) UV-vis absorption spectrum of the HfS_2 flakes on mica. The inset shows the fitting curve for obtaining the bandgap. Reprinted with permission from [85], B. Zheng, et al., *2D Mater.* 3, 035024 (**2016**). © 2016, IOP Publishing; From [82], L. Fu, et al., *Adv. Mater.* 29, 1700439 (**2017**). © 2017, Wiley-VCH; From [87], C. Yan, et al., *Adv. Funct. Mater.* 27, 1702918 (**2017**). © 2017, Wiley-VCH.

for the calculations. The calculated electronic structures of mono-, bi-, tri-, quad-layer and bulk HfS_2 are represented in Figure 2(a).[85] It is found that the direct excitonic transitions occur at Γ point and the indirect from Γ point to M point. With decreasing layer thickness, both direct and indirect bandgaps become larger, from 2.7 eV to 3.0 eV and 1.7 eV to 2.3 eV, respectively, suggesting that the few-layered HfS_2 with different thicknesses will broaden the absorption range. The strong absorption based on direct and indirect transitions implies potential applications of HfS_2 layer in optoelectronic devices.

Bandgap of HfS_2 can also be experimentally obtained via photoluminescence (PL) spectroscopy. As can be seen from the PL spectra of HfS_2 flakes synthesized on mica substrates (Fig. 2(b)), the near-bandgap emission of HfS_2 is located at around 1.43 eV.[82] To eliminate the interference of the strong fluorescence peak from mica, Yan et al. transferred the HfS_2 layers from mica to SiO_2/Si substrate via the dry-transfer approach.[87] As shown in Figure 2(c), the upper line displays the PL spectrum of the HfS_2 flake with a primary peak at 580 nm (2.07 eV) and two weak peaks at 590 nm and 640 nm. The primary peak corresponds to the near-bandgap emission of HfS_2, whereas the two weak peaks are most likely associated with the defect-related emission. Additionally, the PL spectrum of HfS_2 measured on *c*-sapphire substrate by Wang et al. displays two entirely different peaks: a primary peak at 470 nm (2.64 eV) attributed to the near-bandgap emission, and a shoulder peak at 490 nm (2.53 eV) most likely associated with the defect-related emission.[86]

UV-vis absorption spectroscopy is another concise and effective method for investigating the intrinsic optical bandgap of ultrathin 2D materials. Figure 2(d) shows the UV-vis absorption spectrum of HfS_2 layers on the highly transparent mica substrate measured by Yan et al.[87] An obvious absorption edge at 450 nm can be observed in the UV-vis absorption spectrum, indicating the presence of an optical bandgap. As a typical indirect bandgap semiconductor, the optical bandgap of HfS_2 layer is estimated to be about 2.0 eV based on the Tauc's relationship. In addition, Wang et al. demonstrated the UV-vis absorption spectrum of HfS_2 on *c*-sapphire substrate, and the corresponding bandgap is estimated to be 2.67 eV, close to their PL results.[86] To an extent, the discrepant PL and UV-vis absorption behaviors of 2D HfS_2 on different substrates may be mainly related to the indirect bandgap characteristics of HfS_2, and bandgap variations of HfS_2 by strain engineering.

2.3. Electrical Properties

Due to the very low measured conductivity of HfS_2 compared with that of MoS_2, HfS_2 was previously considered as a semi-insulating material.[38,88,89] However, in recent studies, apart from the sizable bandgap, some

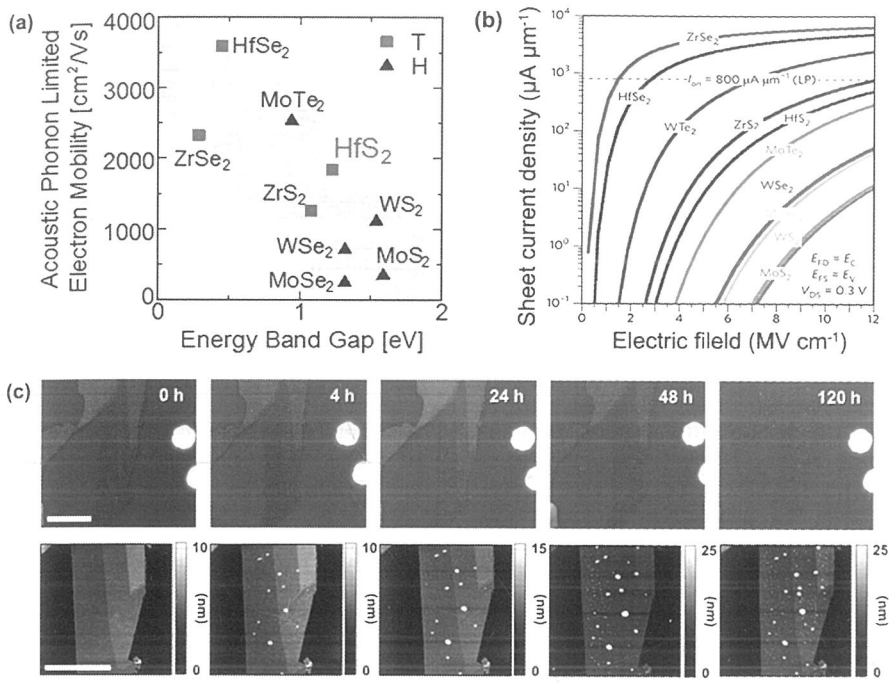

Figure 3. (a) The acoustic phonon-limited electron mobilities as a function of energy bandgap. (b) Simulated sheet current density in abrupt TMDs *p–n* junctions versus junction electric field. The dashed line refers to the I_{on} required for low-power (LP) applications for ITRS 2018. (c) OM (top) and AFM (bottom) images of exfoliated HfS_2 layers with time variation. Scale bar is 10 μm. Reprinted with permission from [79], T. Kanazawa, et al., *Sci. Rep.* 6, 22277 **(2016)**. © 2016, Nature Publishing Group; From [65], G. Fiori, et al., *Nat. Nanotechnol.* 9, 768 **(2014)**. © 2014, Nature Publishing Group; From [78], S. H. Chae, et al., *ACS Nano* 10, 1309 **(2016)**. © 2016, American Chemical Society.

charming electrical properties of single-layered HfS_2 have been theoretically predicted, including excellent carrier mobility and ultrahigh computed sheet currents density. Zhang and co-workers performed the electronic calculations of 1T type materials, and found that the phonon limited mobility is inescapably influenced by three parameters: the sound velocity, the electron–phonon coupling constant, and the electron effective mass.[64] In order to rapidly screen out the materials with high performance, mobility limited by the long wave acoustic phonons are listed in the Figure 3(a). Compared with the other 2D TMDs, HfS_2 shows a large upper bound of acoustic limited mobility over 1800 $cm^2\ V^{-1}\ s^{-1}$, and this value is even five times larger than that of the well-studied MoS_2 (340 $cm^2\ V^{-1}\ s^{-1}$). Although several reports concerning the carrier mobility of MoS_2 suggested the existence of several other scattering mechanisms,[38, 90, 91] the comparison of mobilities in TMDs using the uniform calculation method will aptly represent the relative trend among these mobilities.

The compelling demand for higher performance and lower power consumption in electronic systems is the main driving force for the development of next-generation devices and or architectures based on new materials. Thus, Fiori et al. focused on the challenges of using 2D materials for future digital electronics.[65] It is found that internal fields greatly exceeding the limits of bulk tunnel junctions are feasible, allowing much higher current densities. The computed tunnel current densities for TMDs homojunctions are plotted against electric field for a wide range of TMDs in Figure 3(b). As can be seen from Figure 3(b), HfS_2 based tunneling field-effect transistors (FETs) have a sheet current density of up to 650 $\mu A\ \mu m^{-1}$ (almost 85 times higher than that of MoS_2), appealing for the application of low-power devices. Additionally, large electron affinity of HfS_2 has a possibility to achieve low contact resistance for *n*-type carrier transport because of basic principle of the contact formation between semiconductors and metals.[79] Overall, the above-mentioned superior electronic properties lead layered HfS_2 to have tremendous potential for electronic and optoelectronic applications in the future.

2.4. Chemical Stability

A surface sensitivity study performed on different TMDs in air is quite a significant work to understand which material is the most stable and suitable for application under ambient conditions. Mirabelli et al. reported a systematic research of HfS_2 and other TMDs surfaces in air.[68] The change of surface features is represented by atomic force microscopy (AFM) and scanning electron microscopy (SEM) measurements. Notably, after five months of air exposure, the typical terraced structure of HfS_2 layers is obvious, which is related to the layered structure of the material itself. In addition, the morphology of HfS_2 appears to be quite uniform with no additional

visible blisters or surface change, and the root-mean-square (RMS) roughness is significantly lower than that of other TMDs during the period of study, implying the good air stability of HfS_2 crystal. Lee and co-workers exposed exfoliated HfS_2 layers to air for a given time to investigate their oxidation effect and degradation.[78] Figure 3(c) shows the corresponding optical microscopy (OM) (top panel) and AFM images (bottom panel) for the morphological change of the exfoliated HfS_2 layers transferred onto SiO_2/Si substrate. After a few hours in the air, the thickness of HfS_2 increases gradually, while the surface reveals the presence of small bubbles simultaneously. Further analysis via Raman spectra and transmission electron microscopy (TEM) confirms that Hf atoms react with oxygen molecules and form nearly polycrystalline HfO_x to increase its thickness, which strongly implies that the HfS_2 layer is easily oxidized under ambient conditions. These completely contradictory results on the stability of HfS_2 layers may result from the different humidity in the experimental study, because of the oxidation occurring more severely with humidity. Hence, the more accurate and systematic research related to the chemical stability of HfS_2 should be carried out, which will promote practical applications of HfS_2.

3. SYNTHESIS AND CHARACTERIZATIONS OF 2D HfS_2

Generally speaking, the diverse markets of 2D HfS_2 layer are essentially driven by progress in the preparation of ultrathin HfS_2 layers with desired high crystal qualities and uniform properties, which are quite important for translating their excellent electronic and optical properties into practical applications. Theoretically, analogously to what has been accomplished for graphene,[10] there are probably a dozen methods can be used for preparing 2D HfS_2 with various dimensions, shapes and quality. Here we concentrate only on the two existing top-down mechanical exfoliation and bottom-up chemical vapor deposition (CVD) strategies for synthesizing ultrathin HfS_2 layers, and the advantages and limitations of each method are discussed along with addition of personal insights. After that, we introduce the diverse techniques that have been widely employed for characterizing ultrathin 2D HfS_2 layers.

3.1. Mechanical Exfoliation

The mechanical exfoliation technique is a conventional method to fabricate thin flakes from layered bulk crystals by using Scotch tape, which is firstly adopted by Geim and co-workers to obtain single layer graphene[1] and has been extended to other layered van der Waals materials such as black phosphorus,[11] h-BN[22] and TMDs.[36] The original idea of this technique is to apply mechanical force via Scotch tape to break the weak van der Waals interaction between the layers of bulk crystals without destroying the in-plane covalent bonds of each layer, hence peeling off

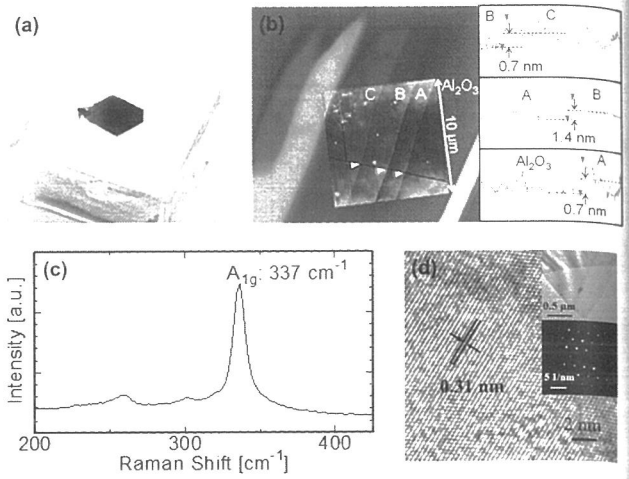

Figure 4. (a) Single crystal piece of HfS_2. (b) OM image and AFM profiles of HfS_2 layers on Al_2O_3, and the inset shows the corresponding AFM height image. (c) Raman spectrum of the exfoliated HfS_2 layer on SiO_2/Si substrate. (d) HRTEM and SAED pattern (inset) images. Reprinted with permission from [79], T. Kanazawa, et al., *Sci. Rep.* 6, 22277 **(2016)**. © 2016, Nature Publishing Group; From [75], K. Xu, et al., *Adv. Mater.* 27, 7881 **(2015)**. © 2015, Wiley-VCH.

single- or few-layered 2D crystals. Theoretically speaking, this technique is capable of producing all kinds of ultrathin 2D materials whose bulk crystals are layered compounds.

In a typical process, the bulk material (HfS_2 crystal, shown in Fig. 4(a)) is first attached to the adhesive on the Scotch tape and then peeled into a thin flake by using another adhesive surface. This process can be repeated again and again in order to obtain an appropriately thin flake. After that, the freshly cleaved thin HfS_2 flake on the Scotch tape is attached to a clean, flat target substrate (e.g., Al_2O_3 substrate) under gentle pressure, and then the Scotch tape is peeled off from the substrate slowly. Finally, the ultrathin single- or few-layered HfS_2 nanoflakes left over on the substrate can be observed and identified by an OM when the suitable substrate are used. Figure 4(b) shows the OM and the corresponding AFM (inset) images of exfoliated HfS_2 flakes on Al_2O_3 substrate with cut line profiles.[79] Due to the narrow bandgap, several layers of HfS_2 are clearly observable by the OM, and the thicknesses could be easily identified by the color of the flakes, as reported in graphene[92] and MoS_2.[93] As extracted from the height profiles (Fig. 4(b)), the steps between the different contrast layers in the inset AFM image are approximately 0.7 nm and 1.4 nm, appearing to be single and double atomic steps, respectively. Mechanical exfoliation technique can be categorized as a nondestructive method because neither chemicals nor chemical reactions are necessary during the fabrication process. Therefore, the exfoliated single- or few-layered HfS_2 nanoflakes keep the "perfect" crystal quality, normally defined as pristine, from their layered bulk crystals.[94] The Raman spectrum of the thin exfoliated HfS_2 layers on the SiO_2/Si substrate measured by Kanazawa et al.[79] is represented in Figure 4(c).

As can be seen from the Raman region, a primary peak appears at the Raman shift of approximately 337 cm^{-1}, which is consistent with the aforementioned A_{1g} first-order mode of bulk HfS_2 crystal. Satellite peaks at 260 cm^{-1} and 321 cm^{-1} are also obtained clearly, considered as the E_g and E_u (LO) modes, respectively. These results indicate that the thin HfS_2 layers with well-aligned atoms remained intact after exfoliation process. Figure 4(d) displays a typical high resolution TEM (HRTEM) image of the thin exfoliated HfS_2 flake.[75] The measured lattice fringes are 0.31 nm, corresponding to the (10–10) plane of 1T phase HfS_2. The selective area electron diffraction (SAED) pattern, as shown in the inset of Figure 4(d), clearly reveals the hexagonal symmetry, and the sharp diffraction spots further indicate the high-quality crystalline structure of the exfoliated HfS_2 flake. All characterizations clarify that ultrathin 2D HfS_2 material prepared via mechanical exfoliation technique remain in the same crystal structures as their bulk crystals and contain excellent crystal quality with minimum defects.

Overall, the mechanical exfoliation technique possesses many advantages, such as high crystal quality, clean surface, and excellent operability, which make the mechanically cleaved ultrathin 2D HfS_2 compelling candidate for the fundamental research of the intrinsic mechanical, optical and electrical properties, as well as the demonstration of high performance electronic and or optoelectronic devices. However, there are still several important drawbacks that restrict its practical applications in its current form. First, ultrathin layers obtained by mechanical exfoliation are in a great minority among accompanying thicker flakes, making the production rate and yield of this technique are quite low. Consequently, this technique cannot meet the demands of various actual applications for which large amounts of materials are required. Second, the shape, the size, and the thickness of the prepared ultrathin 2D HfS_2 layers are difficult to control because the exfoliation process is operated artificially by hands, which lack the controllability, repeatability, and precision. Lastly, this technique is only applicable to materials for which large, layered crystals are available.

3.2. Chemical Vapor Deposition

Over the past decade, CVD technique has been continuously developed and recognized as a reliable and powerful method for preparing a large number of ultrathin 2D materials.[94] Initially, amorphous SiO_2/Si substrates are utilized for TMDs synthesis due to their excellent compatibility with Si-based electronics.[95] Recently, HfS_2 nanosheets have been grown on SiO_2/Si substrate using hafnium chloride ($HfCl_4$) and sulfur powders as the reactants via CVD method by Chen and co-workers.[85] Typically, the cleaned SiO_2/Si substrates are loaded into the CVD system with two independently controlled temperature zones, as illustrated in Figure 5(a), and placed at the downstream heating zone of the furnace. Two crucibles containing $HfCl_4$

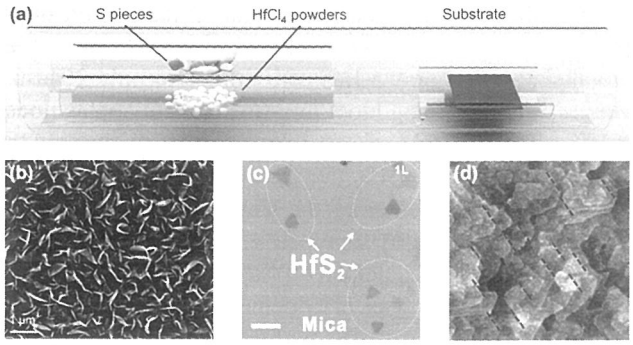

Figure 5. (a) Schematic illustration of CVD synthesis of HfS_2 on substrate in a two zone furnace. (b) SEM image of the vertically oriented HfS_2 nanosheets on SiO_2/Si. (c) Bright field OM images of the HfS_2 crystals on mica. Scale bar is 50 μm. (d) The typical AFM image of the CVD-grown HfS_2 layer on sapphire, showing a regular terraced structure with the terrace edges parallel to each other. Reprinted with permission from [85], B. Zheng, et al., *2D Mater.* 3, 035024 (**2016**). © 2016, IOP Publishing; From [82], L. Fu, et al., *Adv. Mater.* 29, 1700439 (**2017**). © 2017, Wiley-VCH; From [86], D. G. Wang, et al., *2D Mater.* 4, 031012 (**2017**). © 2017, IOP Publishing.

and sulfur powders are respectively put inside two small quartz tubes and located at the upstream heating zone of the furnace. During the growth, the upstream heating zone is set at 160 °C, while the downstream zone is kept at 950 °C. After the synthesis of HfS_2, all heating is stopped and the furnace is opened rapidly to cool down. Nevertheless, due to the high interlayer interaction energy of HfS_2 and the dangling bonds at the surface of SiO_2/Si, the vertically oriented HfS_2 nanosheets are obtained on SiO_2/Si substrate, as shown in Figure 5(b). Obviously, these vertically oriented HfS_2 nanosheets with very rough surface are not suitable for fabricating electronic devices. To bring more opportunities for the actual applications, ultrathin large-area HfS_2 layers with smooth morphology and good structural quality are highly desirable.

More recent studies have revealed that insulating single crystals including sapphire, mica and quartz can also be applied to prepare high-quality 2D TMDs.[96–99] The advantage of using these single crystal substrates lies in their rather outstanding thermal stability and glorious chemical inertness, and the flat surface may also potentially facilitate precursor migration during the CVD process, thereby improving the thickness uniformity of resulting TMDs layers.[95] Almost simultaneously, Fu et al.[82] and Yan et al.[87] carried out the growth of HfS_2 domains on mica substrate, respectively. To adjust reactant concentrations and diffusion rate for the controllable growth of HfS_2, Fu et al. employed a mechanical device to rapidly move the resources to RT area when the reaction has just terminated, whereas Yan et al. introduced a confined space realized by inserting an inner quartz tube to establish a stable laminar flow. Figure 5(c) illustrates the typical OM image of as-grown HfS_2 domains on mica substrate with the regularly triangular and hexagonal shapes, implying that the as-prepared HfS_2 is single crystalline domain. Significantly,

the growth of 2D HfS_2 single-crystal domains with high quality has been achieved on mica substrates. However, the lateral sizes of as-grown HfS_2 are limited to only 20 μm, which is the stumbling block for the practical applications of HfS_2. Thus far, numerous efforts should been devoted to synthesize large-size HfS_2 domains on various substrates.

Additionally, considering the tiny lattice mismatch of 0.84% (using a (6×6) supercell of HfS_2 rotated by 30° to match a (4×4) supercell of sapphire) between HfS_2 and *c*-sapphire, Wang et al.[86] demonstrated the epitaxial growth of high-quality HfS_2 with a controlled number of layers on sapphire substrates by CVD method. Figure 5(d) shows the typical AFM height image of CVD-grown HfS_2 layers on the sapphire substrate. The surface of HfS_2 is rather smooth with a RMS roughness of 0.45 nm, and an intrinsic regular terraced structure with sharp edges can be observed clearly in Figure 5(d). More interestingly, a careful examination of the AFM image reveals that most of the terrace edges are oriented along a dominant direction (the parallel blue dashed lines in Fig. 5(d)), evidencing the epitaxial relationship between HfS_2 and *c*-sapphire. In the end, based on the X-ray diffraction (XRD) and cross-sectional HRTEM measurements, the researchers confirm that the HfS_2 layers exhibit an atomically sharp interface with *c*-sapphire, and the epitaxial relationship between the HfS_2 layers and sapphire substrate is determined to be: HfS_2 (0001) [10–10] ‖ sapphire (0001) [1–100].

In generally, the substrate temperature plays an important role in the CVD deposition of TMDs. Here, Yan et al. systematically studied the growth behavior of HfS_2 domains under different deposition temperatures.[87] The OM images of as-grown HfS_2 with deposition temperature at (800, 850, 900, 940, and 980 °C) are shown in Figures $6(a_1)$–(e_1), respectively. When the temperature is set at 800 °C, nanoparticles and a few triangular domains are synthesized with the thickness of a dozen of nanometers (Fig. $6(a_2)$). With the temperature increases from 800 °C to 900 °C, both the nucleation density and the thickness of HfS_2 reduce, whereas the average size of as-synthesized domains increases to around 4 μm. Moreover, the corresponding AFM images (Figs. $6(a_2$–$c_2)$) reveal that the HfS_2 morphologies evolve from irregular triangular to circle and triangular shapes with tilt edges, further to a regular hexagon shape. With increasing the temperature up to 940 °C even to 980 °C, the researchers acquire multilayered truncated triangular HfS_2 domains by screw dislocation-driven growth (shown in Fig. $6(e_2)$). In addition, Fu et al. adjust the evaporation temperature of hafnium source to obtain a specific shape.[82] Triangular HfS_2 domains can be observed dominantly at the low evaporation temperature of 160 °C. With the $HfCl_4$ evaporation temperature increasing to 175 °C even to 190 °C, the shape of the HfS_2 varies from triangle to truncated triangle and to hexagon, which is attributed to the kinetic modulations at far-from equilibrium conditions.

The CVD technique is an effective bottom-up method to obtain ultrathin 2D HfS_2 layers on diverse substrates. Unlike the low yield and production rate of the mechanical exfoliation technique, CVD is capable of producing ultrathin 2D HfS_2 in industry scale, which is promising candidate for the fabrication of high-performance electronic and optoelectronic devices in the future. Even so, the CVD technique still has some disadvantages at its current form. One is that the electronic properties of CVD-synthesized 2D HfS_2 material are quite lower than the theoretically predicted values, thus hindering its potential applications. The other is that the CVD technique normally needs high temperature and inert atmosphere, leading to the relatively high cost of production.

3.3. Characterizations

Along with the rapid development of nanoscience and nanotechnology, many reliable and powerful characterization techniques have been developed for characterizing ultrathin 2D materials to uncover their morphology, composition, electronic states, crystal phase, quality, and

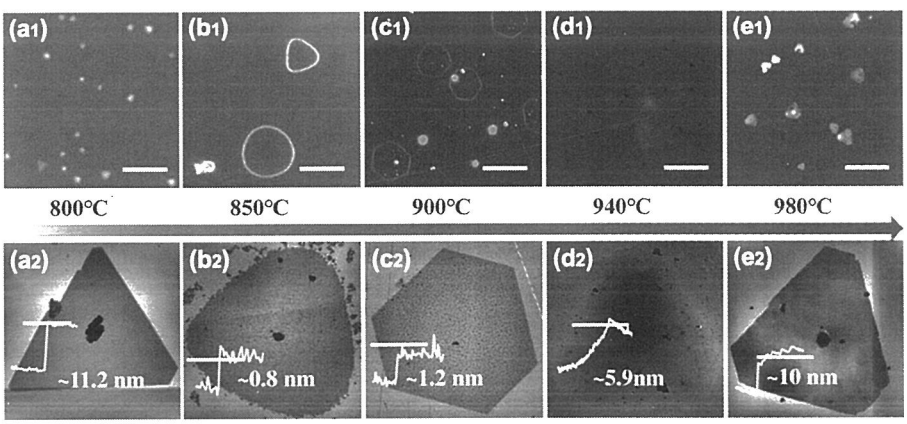

Figure 6. $(a_1$–$e_1)$ Optical images of HfS_2 flakes on the mica at 800, 850, 900, 940, 980 °C, respectively. Scale bar is 10 μm. $(a_2$–$e_2)$ The corresponding AFM images. Reprinted with permission from [87], C. Yan, et al., *Adv. Funct. Mater.* 27, 1702918 **(2017)**. © 2017, Wiley-VCH.

defects.[94] Especially, ultrathin 2D materials obtained by different methods possess various structural characteristics. Therefore, a clear and accurate characterization is of quite importance in uncovering the strong correlation between their structural characteristics and physical properties. Until now, diverse advanced characterization techniques have been widely used to characterize thin 2D HfS_2 layers.

Among the diverse techniques, OM is the easiest and most effective method to provide information on shape, thickness, and location of 2D HfS_2 layers. This imaging method is based on the interference of the reflected light. An optical contrast between the bare substrate and 2D HfS_2 is generated when the sample introduces a noticeable perturbation of optical path, which can be applied to identify the thickness of HfS_2 layer in Figures 4(b)[79] and 5(c).[82] However, the diffraction limits the resolution of OM measurement only to around 1 μm, and much more fine structural features cannot be recognized via this technique. SEM is another useful technique to obtain the morphology and surface structure of HfS_2 materials. Unlike the OM, SEM has a much higher spatial resolution because of the small de Broglie wavelength of electrons, and the resolution of the SEM is normally less than 50 nm. For instance, Chen and co-workers employed the SEM to examine the detailed structure of vertically oriented HfS_2 nanosheets.[85] As demonstrated clearly in Figures 5(b) and 7(a), the fine surface structure of the as-grown HfS_2 is composed of vertically oriented nanosheets with uniform thickness of around 10 nm and height of around 400 nm. Nevertheless, due to the intrinsic poor electrical conductivity of the substrate, it is very difficult to characterize the ultrathin HfS_2 layers prepared on sapphire or mica substrates via SEM technique.

AFM has been utilized to study the structure and morphology of 2D HfS_2 material at molecular or even atomic resolutions in three dimensions. In AFM system, a sharp tip with a radius of nanometer magnitude is attached to a cantilever. When the tip is close to the surface of HfS_2 layer, electrostatic forces acted on the tip makes the cantilever bend. Then, a laser deflection (caused by the bend) is accurately captured by a photodiode detector to generate an image. Recently, Wang et al.[86] and Fu et al.[82] employed the AFM technique to measure the morphology and thickness of 2D HfS_2 layers, as clearly revealed in Figures 5(d) and 7(b), respectively. Notably, because of the ultrathin nature of layered 2D materials, their apparent thicknesses measured by AFM may be interfered by the chemical contrast between 2D materials and the surrounding substrate.[1, 100, 101] According to this, thin sample with a thickness of 0.68 nm in Figure 7(b) is regarded as a monolayer of HfS_2. Moreover, AFM technique has the advantages of *in situ* measurements in atmospheric or controlled environments without special sample preparation. Thus, AFM is also an effective tool to study the degradation of 2D HfS_2 in air, and the morphological change over time can be used to assess the chemical stability of HfS_2 layer (Fig. 3(d)).[78]

Raman spectroscopy has been proven to be an accurate and noninvasive technique for thickness characterization, as well as a powerful method to study the phonon modes in 2D materials. For HfS_2, three first-order modes: A_{1g} (337 cm^{-1}), E_g (260 cm^{-1}) and E_u (LO) (321 cm^{-1}) can be identified clearly in the Raman spectra of HfS_2 at room

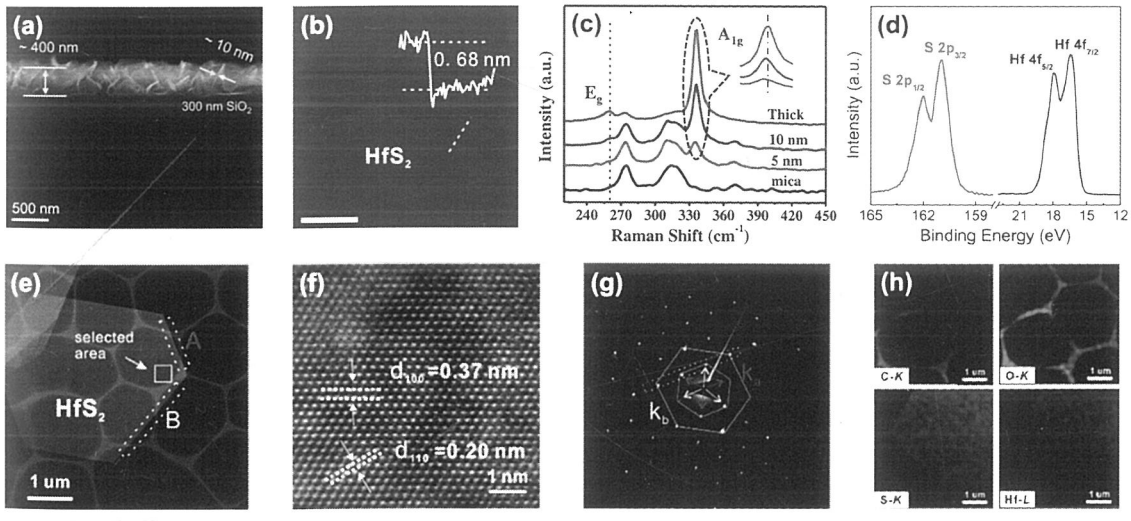

Figure 7. (a) Cross-sectional SEM image of the vertically oriented HfS_2 nanosheets on SiO_2/Si substrate. (b) The thickness of the HfS_2 crystal is 0.68 nm from the AFM cross-sectional profile along the dotted line. Scale bar is 2 μm. (c) Raman spectrum of HfS_2 with different thickness. (d) XPS core-level spectra of S 2*p* and Hf 4*f*. (e) Low-magnification TEM image of an HfS_2 crystal transferred onto a Cu grid. (f) Top-view HRTEM image and (g) the corresponding SAED pattern of HfS_2 crystal. (h) EDS mapping of O–K, C–K, S–K, Hf–L of an HfS_2 crystal, respectively. Reprinted with permission from [85], B. Zheng, et al., *2D Mater.* 3, 035024 **(2016)**. © 2016, IOP Publishing; From [82], L. Fu, et al., *Adv. Mater.* 29, 1700439 **(2017)**. © 2017, Wiley-VCH; From [87], C. Yan, et al., *Adv. Funct. Mater.* 27, 1702918 **(2017)**. © 2017, Wiley-VCH; From [86], D. G. Wang, et al., *2D Mater.* 4, 031012 **(2017)**. © 2017, IOP Publishing.

temperature (RT).[57] However, the non-centrosymmetric clusters induced by defects in the HfS_2 crystal always bring about the disappearance of E_u (LO) Raman mode. As presented in Figure 7(c), a typical Raman spectrum shows two characteristic peaks located at 260.2 cm^{-1} and 336.5 cm^{-1}. The 260.2 cm^{-1} peak is assigned to the E_g mode, corresponding to the in-plane displacement of Hf and S atoms, and the 336.5 cm^{-1} one is the A_{1g} mode, corresponding to the out-of-plane displacement of S atoms. Generally, the phonon frequency of TMDs layers is very sensitive to the thickness. With increasing thickness of crystal, the intensities of both HfS_2 Raman signals significantly increase, which can be ascribed to the addition of the number of scattering centers in the HfS_2 crystal. Notably, caused by the smaller effects of interlayer interactions that induce restoring forces to HfS_2 molecules, the A_{1g} Raman mode develops a slightly red shift from 336.5 cm^{-1} to 334.4 cm^{-1} as the thickness down to 5 nm. Moreover, no detectable Raman signal is obtained when the thickness is lower than 5 nm, probably due to the oxidation and degradation of ultrathin HfS_2 layers.[87] Overall, the sensitivity dependence of the phonon frequency and Raman intensity on the thicknesses of 2D HfS_2 could be a quick and convenient identification of layer numbers.

XPS is a powerful technique that has been widely applied to identify the elemental compositions, electronic states of as-prepared thin 2D HfS_2 layers. To our knowledge, a standard XPS spectrum represents the number of detected electrons as a function of the binding energy of the detected chemical elements within a sample. Due to each element possessing its own characteristic binding energy peaks, the elemental composition can be easily identified from the full XPS spectrum. Moreover, the shape and location of characteristic peaks for each element are very sensitive to the electron configuration within the atoms, making it very effective to analyze the electronic state.[94] As shown in Figure 7(d), XPS technique was utilized by Wang et al.[86] to analyze the CVD-synthesized HfS_2 layers. The peaks at almost 17.9 eV and 16.4 eV binding energies are attributed to Hf $4f_{5/2}$ and $4f_{7/2}$ core levels, respectively, while the peaks at 162.0 eV and 160.9 eV are assigned to S $2p_{1/2}$ and $2p_{3/2}$ core levels, consistent with the standard spectra for HfS_2 crystal. In addition, based on the relative location of characteristic binding energy peaks, the chemical valences of Hf and S are respectively determined to be +4 and −2. XPS technique can not only qualitatively analyze the elemental compositions, but also be used to quantitatively estimate the stoichiometric ratio of elements within the sample. On the basis of the integrated peak areas in Figure 7(d), the atomic ratio of S to Hf is calculated to be around 2, indicating that the CVD-grown HfS_2 layers own the perfect stoichiometry.

TEM technique can provide comprehensive evidence on the size, thickness, exposed facet, crystallinity, phase, and elemental configuration of a thin HfS_2 material, and it is one of the most widely used techniques for characterization of ultrathin 2D materials.[94,95] Compared to SEM, the electrons in the TEM system are generated from a high voltage (normally used voltage is 200 kV), which have a shorter wavelength, thus leading to a much higher resolution. Low-magnification TEM images can be usually applied to precisely measure the lateral size and roughly study the thickness of the target sample. As can be seen from Figure 7(e), the low-magnification TEM image of a typical hexagonal HfS_2 domain transferred on the copper grid is carried out by Fu et al.[82] The lateral size of HfS_2 is calculated to be around 5 μm, and the thickness can be roughly evaluated as quite uniformity on the basis of the homogeneous contrast. Figure 7(f) displays a representative top-view HRTEM image and corresponding SAED patterns (inset) recorded at an HfS_2 domain. It can be found that the HfS_2 domain exhibits a continuous lattice fringe with the same orientation, and the measured crystal plane distances of 0.37 nm and 0.20 nm correspond to the (10–10) and (11–20) planes of HfS_2, respectively. The corresponding sharp SAED pattern in Figure 7(g) clearly reveals hexagonal symmetry, matching well with the crystal phase of 1T HfS_2. Energy dispersive X-ray spectroscopy (EDS) technique is always used to identify the chemical composition and spatial distribution. As shown in Figure 7(h), the EDS mapping measurements reveal a quite uniform spatial distribution of Hf and S of a corner of the HfS_2 crystal in Figure 7(e). However, the electron irradiation of TEM might induce the decomposition or structure change of ultrathin 2D HfS_2 layers, which should be paid much attention to and can be minimized by selecting a properly accelerating voltage during the measurement.

In addition to the above techniques, XRD, PL, and UV-Vis spectroscopy have also been utilized to characterize 2D HfS_2.[75–87] XRD is a nondestructive analytical characterization method to determine the crystal structure of HfS_2 layers, and the XRD-phi scan can be used to further analyze the epitaxial relationship between the HfS_2 layers and substrates. PL spectroscopy is commonly employed to study the luminescence properties of 2D HfS_2, whereas UV-vis absorption spectroscopy is a concise, effective and non-destructive method for investigating the intrinsic optical bandgap of 2D HfS_2.

4. APPLICATIONS OF 2D HfS_2

Because of the unique structural characteristic, ultrathin 2D HfS_2 has exhibited excellent optical, electronic, physical, and chemical properties, which make it a promising candidate for a rich variety of applications. In this section, we summarize the recent process on the utilization of 2D HfS_2 layers in electronics, optoelectronics and photocatalysts, focusing on the FETs, photodetectors and phototransistors.

4.1. Field-Effect Transistors

One of the major applications of 2D HfS_2 layers is transistors, in which HfS_2 serves as the active layer. Recently, He and co-workers fabricated top-gate HfS_2 FETs with high-k HfO_2 dielectric.[77] HfS_2 FETs with Al and Y as the buffer layer and 5 nm HfO_2 as dielectric are demonstrated, and the on/off ratio is obtained to be 10^5 with the sub-threshold swing (SS) is 95 mV dec^{-1}. Even without any functionalization, the FETs can still exhibit outstanding electrical properties. Further research indicates that the self-functionalization of HfS_2 results in the uniform and continuous HfO_2 film free of pinhole-like defects, thus opening up new exciting opportunities for nanoelectronic devices. To evaluate the potential of 2D HfS_2, Kanazawa et al. introduced the electric double-layer (EDL) gate structure for device measurement.[79] Figure 8(a) illustrates the schematic view of multilayer HfS_2-based device structure, and $LiClO_4$:PEO mixture is utilized as an electrolyte gel for gate modulation. As can be seen from Figure 8(b), ClO_4^- and Li^+ ions can freely wander in the electrolyte, and the electric field is localized near the surface (almost 5 nm). Therefore, the large gate capacitance can be expected without any charge trapping. Figure 8(c) shows the transfer characteristics of the fabricated HfS_2 EDL FETs. Due to the EDL gate operation, the drain current is significantly increased from 0.2 $\mu A\ \mu m^{-1}$ to 0.75 mA μm^{-1}, and the effective mobility of EDL device is roughly calculated to be 45 $cm^2\ V^{-1}\ s^{-1}$, indicating the superior potential of the low contact resistivity of HfS_2 for ultralow power applications.

Chae et al. systematically studied the electrical properties of HfS_2 FETs fabricated in a vacuum cluster with and without h-BN passivation and under ambient conditions.[78] The transfer characteristics in Figure 8(d) indicate that the on-current level of the HfS_2-FETs fabricated in the vacuum cluster is around 200 times higher than that of the devices under ambient conditions. Additionally, the researchers also investigate the stability of HfS_2 FETs in air with and without an h-BN layer, and a stable on/off ratio of almost 10^5 is achieved for more than a week via employing an h-BN passivation layer (Figs. 8(e and f)). Nie et al. initially studied the impact of the metal/HfS_2 interface on the FETs performance.[80] It is found that HfS_2 FETs with Ti/Au contacts show a better electrical performance than that of the devices with Pt electrodes, including a higher mobility, larger on/off ratio, smaller SS, and lower cutoff current. These improvements are attributed to a relatively lower work function for Ti/Au contacts than that for Pt metal contacts. In addition, the researchers evaluated the influence of the surface topography of metal films on the FETs performance, and a smooth morphology can also form good contacts, thus enhancing the electrical device performance.

4.2. Photodetectors

Photodetectors that can convert a light signal into an accurate electrical signal, usually a photocurrent or photovoltage, are significant in the development of a multitude of innovative technologies from a practical perspective. Due to the suitable bandgap and charming carrier mobility,[64] 2D HfS_2 is of great potential in the field of photodetectors. Chen and co-workers[85] initially fabricated the CVD-grown HfS_2-based photodetectors on SiO_2/Si substrates, and the device exhibits a photocurrent of 1.2 nA

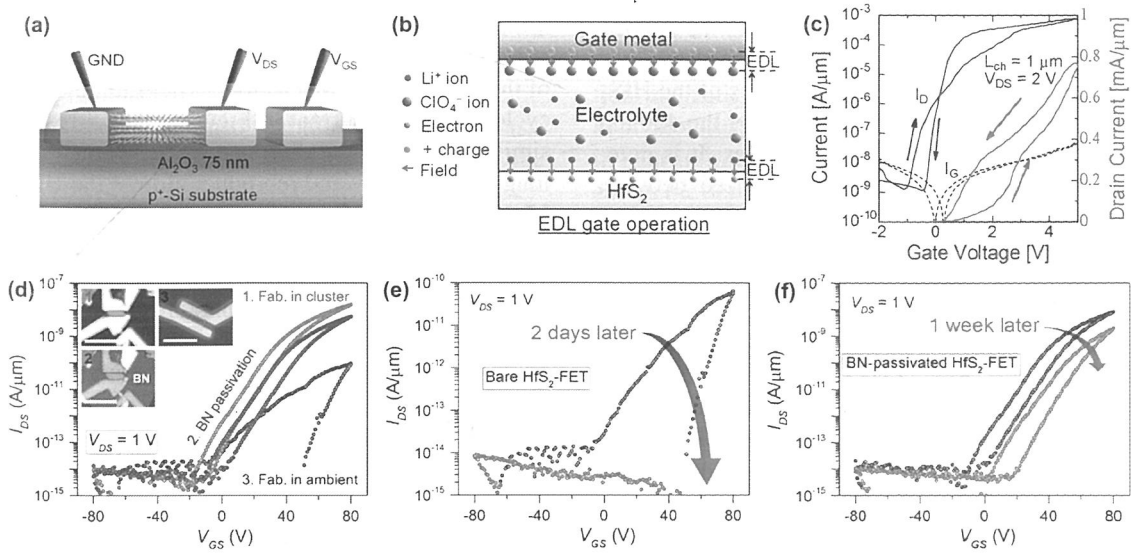

Figure 8. (a) Fabricated EDL transistor, and LiClO4:PEO electrolyte gel is used for the EDL gate. (b) Carrier density modulation by EDL gate operation. (c) Transfer characteristics at V_{ds} of 2 V. (d) Performance comparison for devices fabricated in the cluster (inset 1, red opened line), h-BN-passivated in the cluster (inset 2, blue opened line), and fabricated in air (inset 3, black opened line). Scale bars are 10 μm. Output characteristics of (e) bare HfS_2 and (f) h-BN-passivated HfS_2 devices. Reprinted with permission from [79], T. Kanazawa, et al., *Sci. Rep.* 6, 22277 (**2016**). © 2016, Nature Publishing Group; From [78], S. H. Chae, et al., *ACS Nano* 10, 1309 (**2016**). © 2016, American Chemical Society.

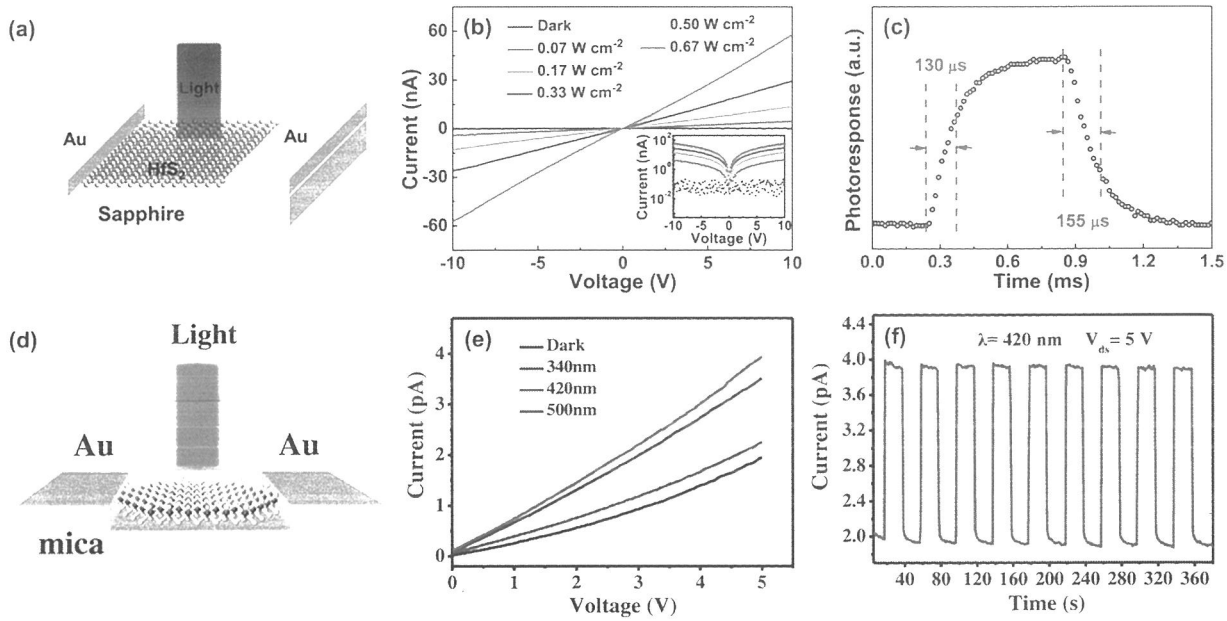

Figure 9. (a) Schematic view of the HfS_2 device structure on sapphire substrate. (b) *I–V* curves of the HfS_2 photodetector measured in the dark and under the 450 nm laser irradiation at various power densities. The inset shows the logarithmic scale of *I–V* curves. (c) Normalized high-resolution photoresponse for rise and fall times. (d) Schematic view of the HfS_2 device structure on mica substrate. (e) *I–V* curves of HfS_2 photodetector measured in the dark and under laser irradiation with varied wavelength ranging from 340 to 500 nm. (f) Time-resolved photoresponse of the device at a bias voltage of 5 V and illumination power of 9.89 mW cm^{-2}. Reprinted with permission from [86], D. G. Wang, et al., *2D Mater.* 4, 031012 **(2017)**. © 2017, IOP Publishing; From [87], C. Yan, et al., *Adv. Funct. Mater.* 27, 1702918 **(2017)**. © 2017, Wiley-VCH.

(power density 0.025 W cm^{-2}, voltage 1 V) for the incident light wavelength at 405 nm. According to the dark current of 1.5 pA, the on/off ratio is calculated to be approach 10^3. Moreover, both the rise and fall times are estimated to be 24 ms. Overall, the device performance based on the vertically oriented few-layered HfS_2 nanosheets is undesirable.

Additionally, photodetectors based on multilayer HfS_2 were prepared by Wang et al.,[86] as illustrated in Figure 9(a). Figure 9(b) shows the *I–V* curves of the HfS_2 photodetectors measured in the dark and under the 450 nm laser irradiation with different power densities. It is noteworthy that excellent Ohmic contact is realized between Au electrodes and HfS_2 layers, indicated by the linear and symmetrical *I–V* curves. As extracted from Figure 9(b), the current under dark and light irradiation (power density 0.67 W cm^{-2}, voltage 10 V) is acquired to be 0.05 nA and 60 nA, resulting in a high on/off ratio of greater than 10^3. Figure 9(c) exhibits the precise *I–t* curve of the multilayer HfS_2-based photodetectors, and the rise and fall times are obtained as short as 130 μs and 155 μs, respectively, indicating an ultrafast response and recovery performance. Responsivity (*R*) is a quite important measure of how efficiently the photodetector converts optical power into photocurrent. Here, the *R* is estimated to around 0.01 mA W^{-1}, which is relatively low, and much more attentions involving improving the crystal quality and optimizing the device architecture should be paid to enhance the device performance.

Yan et al.[87] fabricated the as-grown HfS_2 domains-based photodetectors with Au electrodes constructed via nickel grid shadow method, and the schematic view of the device structure is presented in Figure 9(d). As can be seen from Figure 9(e), the HfS_2 photodetectors exhibit a good photoresponse under a series lasers with ranging wavelengths from 340 nm to 500 nm. Under the 420 nm laser irradiation with power intensity of 9.89 mW cm^{-2}, the maximum *R* is estimated to 2.78 mA W^{-1}, which is larger than that of the aforesaid photodetectors. After multiple illumination cycles, the photocurrent in Figure 9(f) still responded in a similar fashion to the illumination, indicating the excellent long-term stability and reproducibility of the HfS_2 devices. Moreover, the rise and fall times are respectively calculated to be as 55 ms and 78 ms, however, which are quite large and lack of competitive advantage in photodetection. Even so, all aforesaid photoresponse characteristics demonstrate that 2D HfS_2 layers can be effectively used in highly sensitive and fast-switching photodetectors.

4.3. Phototransistors

Recently, He and co-workers have initially demonstrated phototransistors based on the ultrathin exfoliated HfS_2 layer and systematically investigated their optoelectronic properties.[75] It is found that the on/off ratio of HfS_2 devices are strongly dependent on metal contacts, and an excellent on/off ratio of around 10^7 is achieved by using Au contact, which forms lower Schottky barrier with HfS_2 than Cr contact. Through optimizing the flake thickness,

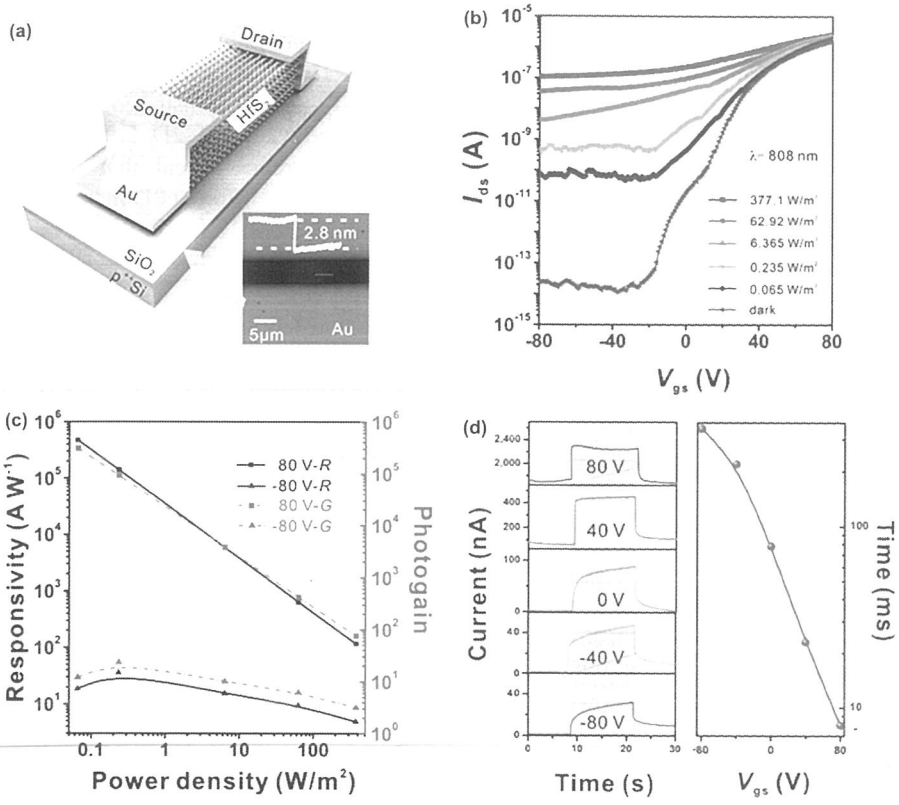

Figure 10. (a) Schematic image of the HfS_2-based back-gated phototransistors. The inset shows an optical image of the HfS_2 device with a thickness of 2.8 nm. (b) Transfer characterizations of the few-layered HfS_2 phototransistors under the 808 nm laser irradiation at various power densities. (c) Responsivity and photogain of HfS_2 phototransistors at V_{gs} of 80 and −80 V. (d) Temporal response of phototransistors under different V_{gs}. The extracted rise time shows a reverse trend corresponding to V_{gs} changing from −80 to 80 V. Reprinted with permission from [82], L. Fu, et al., *Adv. Mater.* 29, 1700439 (**2017**). © 2017, Wiley-VCH.

an ultrahigh R over 890 A W^{-1} and photogain (G) over 2300 (back-gate voltage (V_{gs}) 80 V) are achieved. Moreover, the researchers find the response time exhibits a strong dependence on V_{gs}, and the optimal rise time of almost 38 ms is obtained at the V_{gs} of 80 V.

Unlike the aforementioned phototransistors on basis of the exfoliated HfS_2 layer, Fu et al. fabricated the CVD-grown HfS_2-based transistors on SiO_2/Si substrates.[82] Figure 10(a) presents the schematic image of the back-gated HfS_2 phototransistors, and Au electrodes are constructed via covering copper grid as shadow mask followed by thermal evaporation. The transfer characterizations of HfS_2-based phototransistors in the dark and under the 808 nm laser irradiation with various illumination intensities are illustrated in Figure 10(b). The prominent photoresponse indicates the superior potential of HfS_2 in near-infrared phototransistors applications. Figure 10(c) shows the dependence of R and G on light intensity at V_{gs} of 80 and −80 V for HfS_2 phototransistors, and the maximal R and G are calculated to be as high as 3.08×10^5 A W^{-1}

Table I. Performance comparison of photodevices based on HfS_2 and other 2D materials produced by mechanical exfoliation or CVD method.

Material	Device structure	Fabrication method	Responsivity [mA W^{-1}]	On/off ratio	Rise time [ms]	Fall time [ms]	Mobility [cm^2 V^{-1} s^{-1}]	Ref.
1L MoS_2	Phototransistor	Mechanical exfoliation	7.5	10^3	50	50	0.11	[36]
FL WS_2	Photodetector	CVD method	2.1×10^{-2}	–	5.3	5.3	–	[47]
FL SnS_2	Photodetector	CVD method	9	–	5×10^{-3}	7×10^{-3}	–	[40]
FL ReS_2	Photodetector	CVD method	16.1	10^6	10^3	–	–	[43]
FL HfS_2	Phototransistor	Mechanical exfoliation	8.9×10^5	10^7	38	–	2.4	[75]
FL HfS_2	Phototransistor	CVD method	3.08×10^8	10^8	8	–	7.6	[82]
FL HfS_2	Photodetector	CVD method	–	10^3	24	24	–	[85]
FL HfS_2	Photodetector	CVD method	0.01	10^3	1.3×10^{-1}	1.55×10^{-1}	–	[86]
FL HfS_2	Photodetector	CVD method	2.8	–	55	78	–	[87]

and 4.72×10^5 A W^{-1}, respectively. Furthermore, the rise time of HfS_2 phototransistors as a function of V_{gs} is plotted in Figure 10(d), and the minimal value is estimated to be 8 ms, which is faster than that of phototransistors based on the exfoliated HfS_2 layers.

Additionally, all the significant values for HfS_2-based photodevices compared with those of most other 2D semiconductor are summarized in the Table I. The combination of ultrahigh responsivity, high on/off ratio, fast response time and excellent carrier mobility makes HfS_2 a promising candidate for future high performance optoelectronic devices. Furthermore, 2D HfS_2 has also been predicated to exhibit the potential of being used as photocatalysts for water splitting, because of a wide potential window (−1.8 V to +1.8 V), a large adsorption energy (621.6 kJ mol^{-1}), and a high interaction energy (309.5 kJ mol^{-1}).[69,70]

5. SUMMARY AND OUTLOOK

Within just a few years, huge progress has been achieved in the research area of 2D HfS_2 from the fundamental study to practical applications. In this review, we categorized the recent progress from diverse aspects, that is, the properties, synthesis methods, characterization techniques, and applications. 2D HfS_2 exhibits numerous excellent properties, including decent bandgap, high carrier mobility, extreme sheet current density, and definite chemical stability, which make 2D HfS_2 a potential candidate for a rich variety of applications. Up to now, the mechanical exfoliation and CVD strategies have been used to prepare 2D HfS_2, which have their own advantages and limitations. However, compared to other 2D materials, much more reliable synthesis methods should be developed to obtain 2D HfS_2 layer. With combination of suitable characterization techniques, the composition and structural information on the ultrathin 2D HfS_2 layers can be clearly visualized down to the atomic level, which are quite useful for uncovering the correlations between structures and properties. These charming properties, due to its 2D structural characteristic, have been explored for a variety of applications in the electronics and optoelectronics.

Vast exploration in the field of 2D HfS_2 also brings many new challenges. First, the accurate and systematic researches related to the chemical stability of HfS_2 are insufficient, which should be put much more effort and will further promote industrial device integration of HfS_2. Second, the current production yield, size, and quality of ultrathin 2D HfS_2 are still far from the criteria that are required for practical applications. Therefore, one of the major challenges is to realize the high yield and quality production of 2D HfS_2 to meet the application requirements. Third, the actual utilization of 2D HfS_2 is far from mature and lack of diversity. Currently, the applications of 2D HfS_2 mainly concentrate on the field of FETs, photodetectors and phototransistors, and some specific applications (e.g., catalyst, sensors, solar cells, batteries, supercapacitors, etc.) have not been reported yet and are still challenging. Thus, various devices on the basis of 2D HfS_2 are expected to be demonstrated, which will further enhance the applied value of 2D HfS_2 in the near future. Last, recent researches reveal that heterostructures vertically aligned by two different 2D materials behave with fascinating properties.[3,4,18,102] Therefore, more attention should be paid to the heterostructures assembled by HfS_2 and other 2D materials, which could offer a promising approach to design and fabricate unprecedented devices.

Acknowledgments: This work was financially supported by the National Key Research and Development Program of China (No. 2016YFB0400802), the National Natural Science Foundation of China (Nos. 61674137, U1738114) and the project (No. 17-163-13-ZD-00100302).

References and Notes

1. K. S. Novoselov, A. K. Geim, S. V. Morozov, D. Jiang, Y. Zhang, S. V. Dubonos, I. V. Grigorieva, and A. A. Firsov, *Science* 306, 666 (**2004**).
2. A. K. Geim and K. S. Novoselov, *Nat. Mater.* 6, 183 (**2007**).
3. C. R. Dean, A. F. Young, I. Meric, C. Lee, L. Wang, S. Sorgenfrei, K. Watanabe, T. Taniguchi, P. Kim, K. L. Shepard, and J. Hone, *Nat. Nanotechnol.* 5, 722 (**2010**).
4. A. S. Mayorov, R. V. Gorbachev, S. V. Morozov, L. Britnell, R. Jalil, L. A. Ponomarenko, P. Blake, K. S. Novoselov, K. Watanabe, T. Taniguchi, and A. K. Geim, *Nano Lett.* 11, 2396 (**2011**).
5. S. V. Morozov, K. S. Novoselov, M. I. Katsnelson, F. Schedin, D. C. Elias, J. A. Jaszczak, and A. K. Geim, *Phys. Rev. L* 100, 016602 (**2008**).
6. R. R. Nair, P. Blake, A. N. Grigorenko, K. S. Novoselov, T. J. Booth, T. Stauber, N. M. R. Peres, and A. K. Geim, *Science* 320, 1308 (**2008**).
7. C. Lee, X. Wei, J. W. Kysar, and J. Hone, *Science* 321, 385 (**2008**).
8. F. Liu, P. Ming, and J. Li, *Phys. Rev. B* 76, 064120 (**2007**).
9. A. A. Balandin, *Nat. Mater.* 10, 569 (**2011**).
10. K. S. Novoselov, V. I. Fal'ko, L. Colombo, P. R. Gellert, M. G. Schwab, and K. Kim, *Nature* 490, 192 (**2012**).
11. L. Li, Y. Yu, G. J. Ye, Q. Ge, X. Ou, H. Wu, D. Feng, X. H. Chen, and Y. Zhang, *Nat. Nanotechnol.* 9, 372 (**2014**).
12. L. Li, G. J. Ye, V. Tran, R. Fei, G. Chen, H. Wang, J. Wang, K. Watanabe, T. Taniguchi, L. Yang, X. H. Chen, and Y. Zhang, *Nat. Nanotechnol.* 10, 608 (**2015**).
13. B. Liu, M. Köpf, A. N. Abbas, X. Wang, Q. Guo, Y. Jia, F. Xia, R. Weihrich, F. Bachhuber, F. Pielnhofer, H. Wang, R. Dhall, S. B. Cronin, M. Ge, X. Fang, T. Nilges, and C. Zhou, *Adv. Mater.* 27, 4423 (**2015**).
14. D. Hanlon, C. Backes, E. Doherty, C. S. Cucinotta, N. C. Berner, C. Boland, K. Lee, A. Harvey, P. Lynch, Z. Gholamvand, S. Zhang, K. Wang, G. Moynihan, A. Pokle, Q. M. Ramasse, N. McEvoy, W. J. Blau, J. Wang, G. Abellan, F. Hauke, A. Hirsch, S. Sanvito, D. D. O'Regan, G. S. Duesberg, V. Nicolosi, and J. N. Coleman, *Nat. Commun.* 6, 8563 (**2015**).
15. P. Yasaei, B. Kumar, T. Foroozan, C. Wang, M. Asadi, D. Tuschel, J. E. Indacochea, R. F. Klie, and A. Salehi-Khojin, *Adv. Mater.* 27, 1887 (**2015**).
16. J. Wu, G. K. W. Koon, D. Xiang, C. Han, C. T. Toh, E. S. Kulkarni, I. Verzhbitskiy, A. Carvalho, A. S. Rodin, S. P. Koenig, G. Eda, W. Chen, A. H. C. Neto, and B. Özyilmaz, *ACS Nano* 9, 8070 (**2015**).

17. P. M. Das, G. Danda, A. Cupo, W. M. Parkin, L. Liang, N. Kharche, X. Ling, S. Huang, M. S. Dresselhaus, V. Meunier, and M. Drndić, *ACS Nano* 10, 5687 (**2016**).
18. Z. Yang and J. Hao, *Small Methods* 1, 1700296 (**2017**).
19. Z. Guo, S. Chen, Z. Wang, Z. Yang, F. Liu, Y. Xu, J. Wang, Y. Yi, H. Zhang, L. Liao, P. K. Chu, and X.-F. Yu, *Adv. Mater.* 29, 1703811 (**2015**).
20. M. Bat-Erdene, M. Batmunkh, C. J. Shearer, S. A. Tawfik, M. J. Ford, L. Yu, A. J. Sibley, A. D. Slattery, J. S. Quinton, C. T. Gibson, and J. G. Shapter, *Small Methods* 1, 1700260 (**2017**).
21. K. Watanabe and T. Taniguchi, *Phys. Rev. B* 79, 193104 (**2009**).
22. A. Pakdel, C. Zhi, Y. Bando, and D. Golberg, *Mater. Today* 15, 256 (**2012**).
23. Z. Liu, Y. Gong, W. Zhou, L. Ma, J. Yu, J. C. Idrobo, J. Jung, A. H. MacDonald, R. Vajtai, J. Lou, and P. M. Ajayan, *Nat. Commun.* 4, 2541 (**2013**).
24. C.-H. Lee, T. Schiros, E. J. G. Santos, B. Kim, K. G. Yager, S. J. Kang, S. Lee, J. Yu, K. Watanabe, T. Taniguchi, J. Hone, E. Kaxiras, C. Nuckolls, and P. Kim, *Adv. Mater.* 26, 2812 (**2014**).
25. L. Tan, J. Han, R. G. Mendes, M. H. Rümmeli, J. Liu, Q. Wu, X. Leng, T. Zhang, M. Zeng, and L. Fu, *Adv. Electron. Mater.* 1, 1500223 (**2015**).
26. H. Wang, X. Zhang, J. Meng, Z. Yin, X. Liu, Y. Zhao, and L. Zhang, *Small* 11, 1542 (**2015**).
27. U. Chandni, K. Watanabe, T. Taniguchi, and J. P. Eisenstein, *Nano Lett.* 15, 7329 (**2015**).
28. H. Wang, X. Zhang, H. Liu, Z. Yin, J. Meng, J. Xia, X.-M. Meng, J. Wu, and J. You, *Adv. Mater.* 27, 8109 (**2015**).
29. G. Cassabois, P. Valvin, and B. Gil, *Nat. Photonics* 10, 262 (**2016**).
30. J. Yin, J. Li, Y. Hang, J. Yu, G. Tai, X. Li, Z. Zhang, and W. Guo, *Small* 12, 2942 (**2016**).
31. A-R. Jang, S. Hong, C. Hyun, S. I. Yoon, G. Kim, H. Y. Jeong, T. J. Shin, S. O. Park, K. Wong, S. K. Kwak, N. Park, K. Yu, E. Choi, A. Mishchenko, F. Withers, K. S. Novoselov, H. Lim, and H. S. Shin, *Nano Lett.* 16, 3360 (**2016**).
32. J. Meng, X. Zhang, Y. Wang, Z. Yin, H. Liu, J. Xia, H. Wang, J. You, P. Jin, D. Wang, and X.-M. Meng, *Small* 13, 1604179 (**2017**).
33. A. Azizi, M. R. Gadinski, Q. Li, M. A. AlSaud, J. Wang, Y. Wang, B. Wang, F. Liu, L.-Q. Chen, N. Alem, and Q. Wang, *Adv. Mater.* 29, 1701864 (**2017**).
34. D. He, J. Qiao, L.Zhang, J. Wang, T. Lan, J. Qian, Y. Li, Y. Shi, Y. Chai, W. Lan, L. K. Ono, Y. Qi, J.-B. Xu, W. Ji, and X. Wang, *Sci. Adv.* 3, 1701186 (**2017**).
35. Y. Ji, B. Calderon, Y. Han, P. Cueva, N. R. Jungwirth, H. A. Alsalman, J. Hwang, G. D. Fuchs, D. A. Muller, and M. G. Spencer, *ACS Nano* 11, 12057 (**2017**).
36. Z. Yin, H. Li, H. Li, L. Jiang, Y. Shi, Y. Sun, G. Lu, Q. Zhang, X. Chen, and H. Zhang, *ACS Nano* 6, 74 (**2012**).
37. Q. H. Wang, K. Kalantar-Zadeh, A. Kis, J. N. Coleman, and M. S. Strano, *Nat. Nanotechnol.* 7, 699 (**2012**).
38. M. Chhowalla, H. S. Shin, G. Eda, L.-J. Li, K. P. Loh, and H. Zhang, *Nat. Chem.* 5, 263 (**2013**).
39. D. Jariwala, V. K. Sangwan, L. J. Lauhon, T. J. Marks, and M. C. Hersam, *ACS Nano* 8, 1102 (**2014**).
40. G. Su, V. G. Hadjiev, P. E. Loya, J. Zhang, S. Lei, S. Maharjan, P. Dong, P. M. Ajayan, J. Lou, and H. Peng, *Nano Lett.* 15, 506 (**2015**).
41. Q. Ji, Y. Zhang, Y. Zhang, and Z. Liu, *Chem. Soc. Rev.* 44, 2587 (**2015**).
42. L. M. Xie, *Nanoscale* 7, 18392 (**2015**).
43. M. Hafeez, L. Gan, H. Li, Y. Ma, and T. Zhai, *Adv. Funct. Mater.* 26, 4551 (**2016**).
44. H. Li, C. Tsai, A. L. Koh, L. Cai, A. W. Contryman, A. H. Fragapane, J. Zhao, H. S. Han, H. C. Manoharan, F. Abild-Pedersen, J. K. Nørskov, and X. Zheng, *Nat. Mater.* 15, 48 (**2016**).
45. C. Liu, D. Kong, P.-C. Hsu, H. Yuan, H.-W. Lee, Y. Liu, H. Wang, S. Wang, K. Yan, D. Lin, P. A. Maraccini, K. M. Parker, A. B. Boehm, and Y. Cui, *Nat. Nanotechnol.* 11, 1098 (**2016**).
46. B. Liu, Y. Ma, A. Zhang, L. Chen, A. N. Abbas, Y. Liu, C. Shen, H. Wan, and C. Zhou, *ACS Nano* 10, 5153 (**2016**).
47. N. Perea-López, A. L. Elías, A. Berkdemir, A. Castro-Beltran, H. R. Gutiérrez, S. Feng, R. Lv, T. Hayashi, F. López-Urías, S. Ghosh, B. Muchharla, S. Talapatra, H. Terrones, and M. Terrones, *Adv. Funct. Mater.* 23, 5511 (**2013**).
48. K. Chen, X. Wan, and J. Xu, *Adv. Funct. Mater.* 27, 1603884 (**2017**).
49. K. Kang, K.-H. Lee, Y. Han, H. Gao, S. Xie, D. A. Muller, and J. Park, *Nature* 550, 229 (**2017**).
50. C. Gong, Y. Zhang, W. Chen, J. Chu, T. Lei, J. Pu, L. Dai, C. Wu, Y. Cheng, T. Zhai, L. Li, and J. Xiong, *Adv. Sci.* 4, 1700231 (**2017**).
51. K. Chen, Z. Chen, X. Wan, Z. Zheng, F. Xie, W. Chen, X. Gui, H. Chen, W. Xie, and J. Xu, *Adv. Mater.* 29, 1700704 (**2017**).
52. Q. Zhang, W. Wang, J. Zhang, X. Zhu, and L. Fu, *Adv. Mater.* 30, 1704585 (**2017**).
53. Z. Yu, Z.-Y. Ong, S. Li, J.-B. Xu, G. Zhang, Y.-W. Zhang, Y. Shi, and X. Wang, *Adv. Funct. Mater.* 27, 1604093 (**2017**).
54. J. Zheng, X. Yan, Z. Lu, H. Qiu, G. Xu, X. Zhou, P. Wang, X. Pan, K. Liu, and L. Jiao, *Adv. Mater.* 29, 1604540 (**2017**).
55. P. K. Sahoo, S. Memaran, Y. Xin, L. Balicas, and H. R. Gutiérrez, *Nature* 553, 63 (**2018**).
56. G. Lucovsky, R. M. White, J. A. Benda, and J. F. Revelli, *Phys. Rev. B* 7, 3859 (**1973**).
57. A. Cingolani, M. Lugarà, and F. Lévy, *Physica Scripta* 37, 389 (**1988**).
58. C. Kreis, M. Traving, R. Adelung, L. Kipp, and M. Skibowski, *Appl. Surf. Sci.* 166, 17 (**2000**).
59. M. Traving, T. Seydel, L. Kipp, M. Skibowski, F. Starrost, E. E. Krasovskii, A. Perlov, and W. Schattke, *Phys. Rev. B* 63, 035107 (**2001**).
60. B. Liang and L. Andrews, *J. Phys. Chem. A* 106, 6295 (**2002**).
61. C. Kreis, S. Werth, R. Adelung, L. Kipp, M. Skibowski, E. E. Krasovskii, and W. Schattke, *Phys. Rev. B* 68, 235331 (**2003**).
62. H. L. Zhuang and R. G. Hennig, *J. Phys. Chem. C* 117, 20440 (**2013**).
63. C. Gong, H. Zhang, W. Wang, L. Colombo, R. M. Wallace, and K. Cho, *Appl. Phys. Lett.* 103, 053513 (**2013**).
64. W. Zhang, Z. Huang, W. Zhang, and Y. Li, *Nano Res.* 7, 1731 (**2014**).
65. G. Fiori, F. Bonaccorso, G. Iannaccone, T. Palacios, D. Neumaier, A. Seabaugh, S. K. Banerjee, and L. Colombo, *Nat. Nanotechnol.* 9, 768 (**2014**).
66. J. Kang, H. Sahin, and F. M. Peeters, *Phys. Chem. Chem. Phys.* 17, 27742 (**2015**).
67. F. A. Rasmussen and K. S. Thygesen, *J. Phys. Chem. C* 119, 13169 (**2015**).
68. G. Mirabelli, C. McGeough, M. Schmidt, E. K. McCarthy, S. Monaghan, I. M. Povey, M. McCarthy, F. Gity, R. Nagle, G. Hughes, A. Cafolla, P. K. Hurley, and R. Duffy, *J. Appl. Phys.* 120, 125102 (**2016**).
69. D. Singh, S. K. Gupta, Y. Sonvane, A. Kumarc, and R. Ahujad, *Catal. Sci. Technol.* 6, 6605 (**2016**).
70. R. J. Toh, Z. Sofer, and M. Pumera, *J. Mater. Chem. A* 4, 18322 (**2016**).
71. X. Zhao, C. Xia, T. Wang, X. Dai, and L. Yang, *J. Alloys Compd.* 689, 302 (**2016**).
72. M. Pandey, K. W. Jacobsen, and K. S. Thygesen, *J. Phys. Chem. C* 120, 23024 (**2016**).
73. K. Iordanidou, M. Houssa, G. Pourtois, V. V. Afanas'ev, and A. Stesmansa, *ECS J. Solid State Sci. Technol.* 5, 3054 (**2016**).
74. Q. Zhao, Y. Guo, K. Si, Z. Ren, J. Bai, and X. Xu, *Phys. Status Solidi B* 254, 1700033 (**2017**).

75. K. Xu, Z. Wang, F. Wang, Y. Huang, F. Wang, L. Yin, C. Jiang, and J. He, *Adv. Mater.* 27, 7881 **(2015)**.
76. J. Chang, *J. Appl. Phys.* 117, 214502 **(2015)**.
77. K. Xu, Y. Huang, B. Chen, Y. Xia, W. Lei, Z. Wang, Q. Wang, F. Wang, L. Yin, and J. He, *Small* 12, 3106 **(2016)**.
78. S. H. Chae, Y. Jin, T. S. Kim, D. S. Chung, H. Na, H. Nam, H. Kim, D. J. Perello, H. Y. Jeong, T. H. Ly, and Y. H. Lee, *ACS Nano* 10, 1309 **(2016)**.
79. T. Kanazawa, T. Amemiya, A. Ishikawa, V. Upadhyaya, K. Tsuruta, T. Tanaka, and Y. Miyamoto, *Sci. Rep.* 6, 22277 **(2016)**.
80. X.-R. Nie, B.-Q. Sun, H. Zhu, M. Zhang, D.-H. Zhao, L. Chen, Q.-Q. Sun, and D. W. Zhang, *ACS Appl. Mater. Interfaces* 9, 26996 **(2017)**.
81. T. Kanazawa, T. Amemiya, V. Upadhyaya, A. Ishikawa, K. Tsuruta, T. Tanaka, and Y. Miyamoto, *IEEE Trans. Nanotechnol.* 16, 582 **(2017)**.
82. L. Fu, F. Wang, B. Wu, N. Wu, W. Huang, H. Wang, C. Jin, L. Zhuang, J. He, L. Fu, and Y. Liu, *Adv. Mater.* 29, 1700439 **(2017)**.
83. H. Kaur, S. Yadav, A. K. Srivastava, N. Singh, S. Rath, J. J. Schneider, O. P. Sinha, and R. Srivastava, *Nano Res.* 11, 343 **(2017)**.
84. J. Zhu, S. Xu, J. Ning, D. Wang, J. Zhang, and Y. Hao, *J. Phys. Chem. C* 121, 24845 **(2017)**.
85. B. Zheng, Y. Chen, Z. Wang, F. Qi, Z. Huang, X. Hao, P. Li, W. Zhang, and Y. Li, *2D Mater.* 3, 035024 **(2016)**.
86. D. G. Wang, X. W. Zhang, H. Liu, J. H. Meng, J. Xia, Z. G. Yin, Y. Wang, J. B. You, and X.-M. Meng, *2D Mater.* 4, 031012 **(2017)**.
87. C. Yan, L. Gan, X. Zhou, J. Guo, W. Huang, J. Huang, B. Jin, J. Xiong, T. Zhai, and Y. Li, *Adv. Funct. Mater.* 27, 1702918 **(2017)**.
88. T. J. Wieting, *J. Phys. Chem. Solids* 31, 2148 **(1970)**.
89. L. E. Conroy and K. C. Park, *Inorg. Chem.* 7, 459 **(1968)**.
90. S. Kim, A. Konar, W.-S. Hwang, J. H. Lee, J. Lee, J. Yang, C. Jung, H. Kim, J.-B. Yoo, J.-Y. Choi, Y. W. Jin, S. Y. Lee, D. Jena, W. Choi, and K. Kim, *Nat. Commun.* 3, 1011 **(2012)**.
91. X. Li, J. T. Mullen, Z. Jin, K. M. Borysenko, M. B. Nardelli, and K. W. Kim, *Phys. Rev. B* 87, 115418 **(2013)**.
92. P. Blake, E. W. Hill, A. H. Castro Neto, K. S. Novoselov, D. Jiang, R. Yang, T. J. Booth, and A. K. Geim, *Appl. Phys. Lett.* 91, 063124 **(2007)**.
93. A. Castellanos-Gomez, N. Agraït, and G. Rubio-Bollinger, *Appl. Phys. Lett.* 96, 213116 **(2010)**.
94. C. Tan, X. Cao, X.-J. Wu, Q. He, J. Yang, X. Zhang, J. Chen, W. Zhao, S. Han, G.-H. Nam, M. Sindoro, and H. Zhang, *Chem. Rev.* 117, 6225 **(2017)**.
95. Q. Ji, Y. Zhang, Y. Zhang, and Z. Liu, *Chem. Soc. Rev.* 44, 2587 **(2015)**.
96. Y. Zhang, Y. Zhang, Q. Ji, J. Ju, H. Yuan, J. Shi, T. Gao, D. Ma, M. Liu, Y. Chen, X. Song, H. Y. Hwang, Y. Cui, and Z. Liu, *ACS Nano* 7, 8963 **(2013)**.
97. Y. Yu, C. Li, Y. Liu, L. Su, Y. Zhang, and L. Cao, *Sci. Rep.* 3, 1866 **(2013)**.
98. Q. Ji, Y. Zhang, T. Gao, Y. Zhang, D. Ma, M. Liu, Y. Chen, X. Qiao, P.-H. Tan, M. Kan, J. Feng, Q. Sun, and Z. Liu, *Nano Lett.* 13, 3870 **(2013)**.
99. J.-K. Huang, J. Pu, C.-L. Hsu, M.-H. Chiu, Z.-Y. Juang, Y.-H. Chang, W.-H. Chang, Y. Iwasa, T. Takenobu, and L.-J. Li, *ACS Nano* 8, 923 **(2014)**.
100. A. C. Ferrari, J. C. Meyer, V. Scardaci, C. Casiraghi, M. Lazzeri, F. Mauri, S. Piscanec, D. Jiang, K. S. Novoselov, S. Roth, and A. K. Geim, *Phys. Rev. L* 97, 187401 **(2006)**.
101. K. Xu, P. Cao, and J. R. Heath, *Science* 329, 1188 **(2010)**.
102. A. K. Geim and I. V. Grigorieva, *Nature* 499, 419 **(2013)**.

Received: 3 January 2018. Accepted: 22 March 2018.